Electrochimica Acta 441 (2023) 141754

Contents lists available at ScienceDirect

Electrochimica Acta

journal homepage: www.journals.elsevier.com/electrochimica-acta

Optimizing anion storage performances of graphite/ non-graphitic carbon composites as cathodes for dual-ion batteries

Shuvajit Ghosh, Nihad MP, Sadananda Muduli, Subhajit Bhowmik, Surendra K. Martha *

Department of Chemistry, Indian Institute of Technology Hyderabad, Kandi, Sangareddy, 502284, Telangana, India

ARTICLE INFO

Keywords:
Anion intercalation
Graphite cathode
Carbon composite
Electrochemical optimizations
Dual-ion cell

ABSTRACT

Anion intercalation capacity of graphite cathode is a limiting factor towards the development of dual-ion energy storage devices. A large portion of electrochemically active sites in graphite lattice remains inaccessible to anions due to the instability of electrolytes beyond 5 V. Strategy to composite graphitic intercalation along with surface storage from non-graphitic carbons to enhance capacity is explored in this work. Optimizations are performed to determine the best ratio of graphitic and non-graphitic carbons, and to find out the blend of physical properties of non-graphitic carbons that aid the surface contribution to the greatest extent. Besides, it is also optimized to obtain the maximum achievable lifetime and efficiency, suitable active material loading for balancing energy-power output, and the safest upper cut-off voltage for trading off capacity against cycle life. Surface area, pore size, functional groups, and doped elements govern the electrochemical properties of non-graphitic carbons. A composite of graphite with high surface area carbon (2477 $m^2\ g^{-1}$) in a 75:25 ratio doubles the capacity, whereas the composite of graphite and reduced graphene oxide at the same ratio yields prolonged cycle life at 100 mA g^{-1} within 2.0–5.0 V. The capacity improvement is invariably reproducible in dual carbon cell using composite materials as both electrodes.

1. Introduction

The urgency of gigawatt-scale energy storage needs no elaboration. Lithium-ion batteries (LIBs) have been leading the portable electronics market for the last three decades. However, implementing it in all sectors of energy storage has raised grave concerns recently [1–3]. Conventional LIBs are the state-of-the-art system for most of the applications, whereas next-generation analogs (Na, K, Al, etc.) and solid-state devices may surpass conventional LIBs as cheaper, safer, and sustainable alternatives in no-distant future [4–6]. The drawbacks mainly originate from cathode due to the production issues and performance limitations. Cathode material contains transition metals (Ni, Co, Mn, Cu, etc.) which are costly, scarce, heavy, and toxic to the human body. The usage of cobalt is highly disregarded by the community owing to geopolitical conflicts centered on mining [7,8]. Packing a high amount of nickel in order to go cobalt-free and to boost energy density is dwindling down its reserve at a thundering pace [9]. The cost of raw lithium also fluctuates due to the irregularities in supply chain [10]. Therefore, the unpredictability in raw material availability and cost affect the market price stability of large LIB modules [11]. From the performance point of view, oxygen release from cathode lattice during electrochemical cycling at high voltage ($\geq$ 4.5 V vs. Li^+/Li) raises safety stakes even with solid electrolytes [12–15]. Hence, shrugging off the transition metal dependence by replacing it with carbon is a beneficial option in terms of safety, sustainability, cost, and recyclability [16,17]. Moreover, the cell functioning on carbon as active material at both electrodes is possible to fabricate indigenously in the countries which do not have a stronghold on lithium and transition metal mines. The carbon cathode accommodates anion along with simultaneous storage of cation in anode during charge and releases it back to electrolyte during discharge. Optimizing the anion storage performance of carbon cathode is one of the key aspects of developing dual-ion batteries [18,19].

Graphite is the best material in terms of capacity as bulky anions need the support of two perfectly oriented graphene sheets to form a stable intercalation compound. The onset potential of anion intercalation into graphite is $\geq$ 4.5 V. The electrochemically active voltage region is confined to 4.5 – 5.0 V resulting in capacity in the range of 20 – 65 mAh g^{-1} for PF_6^- storage depending upon the physical characteristics of graphite, type and properties of electrolyte, temperature of electrochemical cycling, etc. [20,21]. Hence, the capacity shortfall is one of the

* Corresponding author.
E-mail address: martha@chy.iith.ac.in (S.K. Martha).

https://doi.org/10.1016/j.electacta.2022.141754
Received 7 November 2022; Received in revised form 12 December 2022; Accepted 21 December 2022
Available online 23 December 2022

major roadblocks behind the practical realization of dual ion cells. Explored approaches in the literature to enhance capacity can be categorized into 3 sections – technical manipulation, electrolyte modification, and material level alteration. Harsh testing conditions like higher temperature (> 40 °C) and widened upper charge cut-off voltage (> 5.0 V) yield better capacity, but it comes with a disadvantage of accelerated electrolyte decomposition [22]. Advanced electrolytes such as ionic liquids, highly concentrated salt, and conventional electrolytes with smaller anion and high-voltage additives are able to provide higher capacity [23–26]. However, imide-based ionic liquids cannot form a protective film on graphite anode surface and, thereby difficult to use in dual carbon cells [27]. Further, the cost of concentrated electrolytes (≥ 3 M) is higher than conventional prototypes. The focus on electrolyte modification is out of the scope of this study. Material level variations are mainly pursued here. Anion intercalation capacity of graphite is site limited. Number of sites to incorporate anions are fixed, and the major portion remains inaccessible in the squeezed voltage range of intercalation i.e., 4.5–5.0 V. Tuning physical properties of graphite by reducing particle size, inducing porosity, increasing surface area, etc. can improve the capacity by improving storage at exposed surfaces and edge-sites but the overall percentage of increment is low [28–30]. Non-graphitic carbons containing doped heteroatoms, surface functional groups and having higher surface area are better matrices to extract surface capacity. Herein, we investigate a strategy of compositing graphite with non-graphitic carbons to leverage the synergistic benefits of graphitic intercalation beyond 4.5 V and surface storage by non-graphitic carbons below 4.5 V range. Anion storage in non-graphitic carbons and the role of functional heteroatoms, the two underexplored areas in the field have been studied here.

Improvement in the anion storage capacity of graphite by several methods discussed here is summarized in Table S1. Direct comparison among absolute values seems impractical as a different sets of standards is followed in various publications. Existing loopholes in the literature include the usage of thin electrodes (≤ 3 mg cm^{-2}), cycling at higher temperatures to showcase enhanced capacity, and reporting cell life only in number of cycles. The runtime of 1000 cycles may be extended up to 2–3 years for conventional LIBs, while it takes a maximum of 1–2 weeks for capacitors under usual testing conditions. Dual-ion batteries stand somewhere between traditional batteries and electric double-layer capacitors in terms of cycling time [31]. The time range to cover a certain number of cycles dictates the utility of an energy storage device for different applications. Therefore, it is necessary to report the time period and the number of cycles for the more practical assessment. This work is focused on optimizing the anion storage performance of the composite of graphitic/ non-graphitic cathode at a high loading of 10±0.5 mg cm^{-2} using conventional electrolyte, i.e., 1 M $LiPF_6$ in a 1:1 ratio of EC-DEC and on revealing the timespan of long-term cycling performance. Optimizations performed here to balance electrochemical properties are segregated into 5 types (Scheme 1). Each type is systematically studied to elucidate the effectiveness of the compositing approach. Optimization 5 is explained in supplementary material.

2. Experimental

2.1. Materials synthesis

Graphene oxide (GO), reduced graphene oxide (rGO), and orange peel-derived B, N- doped carbon (BNC) are synthesized according to the literature reported methods [32–34]. High surface area carbon (HSC) and graphite is commercially availed from China Steel Corporation, Taiwan.

2.1.1. Synthesis of GO

GO is synthesized according to Hummers method [32]. In a round bottom flask, 500 mg of Graphite powder (China Steel Corporation, Taiwan) and 500 mg of sodium nitrate ($NaNO_3$; Sigma-Aldrich) are mixed with 23 mL of reagent grade sulfuric acid (H_2SO_4; SRL, India). The mixture is stirred in an ice bath for 4 h. Potassium permanganate ($KMnO_4$; Sigma-Aldrich) is added to the solution at a gentle rotation speed. The temperature is kept below 20 °C to avoid overheating. The flask was then shifted to a water bath, maintaining 35 °C temperature, and kept under continuous rotation for 2 h. After that, the mixture is cooled down to 20 °C; 46 mL of deionized water is added slowly via the walls of a glass rod. After that the solution is transferred to a silicone oil bath and refluxed at 100 °C for 2 h. It is cooled to room temperature and diluted using 100 mL of deionized water. 10 mL of 30% hydrogen peroxide (H_2O_2; TCI Chemicals, Japan) is added to it dropwise under stirring conditions. Finally, the solution is taken into a beaker, washed with 5% aqueous HCl solution for several times until the supernatant solution looks clear. The clear solution is decanted. The remained mixture is dried within a petri dish under vacuum at 65 °C for overnight. The obtained chocolate brown colored powder is GO.

2.1.2. Synthesis of rGO

rGO is synthesized according to literature reported method [33]. GO is chemically reduced by iron (II) chloride tetrahydrate ($FeCl_2{\cdot}4H_2O$; Sigma-Aldrich). 150 mg of GO is ultrasonicated in 150 mL of deionized water. Iron (II) chloride solution is prepared by mixing 1.8 g in 180 mL of 5% aqueous HCl solution. These two solutions are mixed and stirred for 24 h at 95 °C. The black precipitate is filtered, washed with deionized water and ethanol, and dried to obtain rGO.

2.1.3. Synthesis of B, N-doped carbon from orange peel (BNC)

B, N-doped porous carbons are synthesized as per our previous report [34]. Peel of orange fruit (*Citrus x Sinensis*) is chosen as a biowaste precursor. It is collected, washed with warm water, dried at 80 °C for 5 days, and grounded to powdery form. 10 g of the powder is mixed with 30 mL 0.1 M boric acid (H_3BO_3; TCI Chemicals) solution, stirred at 60 °C for 3 h, dried at 80 °C for 24 h, followed by calcination in a tubular furnace (Thermoconcept, Germany) at 800 °C for 3 h under argon atmosphere. The calcined powder is stirred in 3 M HCl to remove all the impurities and washed with deionized water until the pH of the solution becomes neutral. Then the sample is vacuum dried at 80 °C to obtain B, N-doped porous carbon.

2.1.4. Preparation of composites

Appropriate ratios (25:75, 50:50, 75:25) of graphite powder and non-graphitic carbons are mixed thoroughly using ball milling (1:25 wt. ratio of solid powder to zirconia balls) in ethanol for 30 h at 200 rpm with intermittent rest. The milled mixture is dried at 100 °C under vacuum for 12 h, and it is ready to be used as active material. The composites are denoted in the following manner – the type of non-graphitic carbon followed by the amount of non-graphitic carbon in the mixture. For an example, HSC25 refers to the composite of 25% HSC with 75% graphite.

2.2. Physical characterizations

The powder X-ray diffraction data of synthesized materials are measured using X' Pert Pro-diffractometer (Netherlands) having θ-θ reflection geometry, CuKα radiation (40 mA, 40 kV) with λ = 1.5406 Å and within a 2θ range of 5°- 70° Raman spectroscopy was performed using Bruker Senterra micro-Raman spectrometer (Bruker Optic GmbH, Ettingen, Germany) equipped with He-Ne laser (532 nm) source. Data are collected at backscattering configuration in the range of 1200–3200 cm^{-1}. The surface area measurement and pore size analysis are carried out through nitrogen adsorption and desorption studies using Autosorb-iQ (Quantachrome Instruments, USA) Brunauer-Emmett-Teller (BET) analyzer. X-ray Photoelectron Spectroscopy (XPS) studies are performed using ESCA+, (Omicron nanotechnology, Oxford Instruments Plc., Germany) equipped with monochromic AlKα (1486.6 eV) X-ray beam radiation operated at 15 kV and 20 mA. The binding energy was

calibrated vs. carbon (C1s = 284.6 eV). The XPS spectra are deconvoluted using the Gaussian function using Origin Software. The morphology of materials is visualized using field emission scanning electron microscopy (FESEM, JEOL-JEM 2011).

2.3. Electrochemical measurements

2.3.1. Slurry and electrode preparation

Composite of graphite and non-graphitic carbon is used as cathode active material. Carbon-coated aluminum foil is used as a positive current collector. The thin carbon coating on Al-surface enables higher loading of the active material. It also protects the surface from pitting under the corrosive environment at high voltages. Electrode composition is maintained to be 90 wt.% active material, 2 wt.% carbon black (Super P C65, Timcal), and 8 wt.% polyvinylidene difluoride (PVDF; KUREHA 1700) and using N-methyl pyrrolidone (NMP; Sigma-Aldrich) as solvent. At first, PVDF is dissolved in NMP solvent, followed by the addition of active material and carbon black to the solution. The slurry is dispersed thoroughly to ensure homogenous mixing. Then the paste is casted on C-coated Al foil using the standard doctor blade technique followed by drying at 90 °C for overnight. Dried electrodes are calendared, manually punched into discs having 12 mm diameter, and stored inside an Ar-filled glovebox (mBraun, Germany) with water and oxygen content < 1 ppm-level. The loading for composite active materials is controlled at 10 ± 0.5 mg cm^{-2} unless specifically mentioned.

2.3.2. Cell fabrication

CR2032 type Li|Graphite cell is fabricated using a composite of graphite and non-graphitic carbon as cathode, 12 mm Li-chip as anode, 16 mm GF/D (Whatman) separator, and 1 M $LiPF_6$ in 1:1 ratio of EC-DEC as electrolyte. The amount of electrolyte used is 100 μL per CR2032 type cell. Dual carbon coin-type cell is also fabricated following a similar process. Prelithiated graphite on copper foil (12 mm diameter) is used as an anode along with composite cathode. The mass ratio of the cathode to anode is maintained at 1.2:1. All cells are given 24 h rest before electrochemical testing.

Single stacked pouch cells are made using 5 × 4 cm^2 electrodes (single anode i.e., composite material on Cu-foil and single cathode i.e., composite material on C-coated Al foil), 5.2 × 4.2 cm^2 of GF/D separator, and 1.3 mL electrolyte. After electrolyte filling, the pouch cells are vacuum-sealed inside the glovebox. It is then kept under pressure within two parallel non-conducting acrylic sheets for 72 h to wet all the interfaces properly. The mass loading ratio of the cathode to anode is 1.2:1. The cathode and anode loading are controlled at 9 ± 0.3 and 7.5 ± 0.3 mg cm^{-2}, respectively.

2.3.3. Electrochemical testing

All galvanostatic charge-discharge cycling studies are conducted in Biologic BCS805 system, data are extracted using BT-Lab software and plotted using Origin software. Each of the electrochemical data reported here is cross-verified against ≥ 5 similar type of cells to ensure reproducibility. All the cycling tests are performed at 25±1 °C temperature. The standard voltage range of testing is 2.0–5.0 V. All voltage values or ranges mentioned in the manuscript are measured against Li^+/Li redox couple. During the C-rate study, 12 h rest is applied between two consecutive current densities to relax the ionic movements. For long-term cycling tests, 10 h rest is applied after a certain number of cycles, which varies depending on the applied current density to maintain the cells in a good state of health. The rest period (10 h rest after every 100 cycles for cycling at 100 mA g^{-1} current density) is excluded from the calculation of overall lifetime. Impedance study is carried out in a battery test unit (Solatron Analytical, Oak Ridge, TN, USA) consisting of 1470E multichannel potentiostat and 1455A frequency response analyzers (FRAs), and data are analyzed through Corrware and ZPlot software from Scribner Associates. The impedance spectrum is recorded in the frequency range between 100 kHz – 10 mHz with a voltage perturbation of 10 mV.

2.3.4. Prelithiation of HSC25

HSC25 coated on copper foil is lithiated electrochemically. The cell is discharged from OCV to 0.01 V vs. Li^+/Li at 20 mA g^{-1} current density. The lithiated electrode is dismantled carefully inside the glove box and utilized for the fabrication of the dual carbon cell. The observed light golden yellow color of the electrode confirms the presence of intercalated lithium inside graphene sheets. However, the exact amount of intercalated lithium is hard to quantify and vastly varies from one cell to another.

3. Results and discussions

3.1. Optimization 1: ratio of graphitic to non-graphitic carbons

HSC is chosen as a model non-graphitic carbon for optimization 1. The composites of graphite and HSC are prepared in 3 ratios – 25:75 (HSC75), 50:50 (HSC50), and 75:25 (HSC25). Average active material loading for composite cathodes is controlled within 5±0.2 mg cm^{-2}. It is difficult to load beyond that level when the HSC percentage is greater than 50% due to its low density. Coated material gets easily peeled off from the current collector surface during electrochemical cycling in case of thicker coating.

The fundamental difference between anion storage properties of pristine graphite and pristine non-graphitic carbons as cathode is presented in Fig S1. The capacity of composite cathodes increases linearly with the percentage of HSC in the composition. HSC25, HSC50, and HSC75 demonstrate discharge capacities of 54, 79, and 101 mAh g^{-1}, respectively, at a current density of 100 mA g^{-1} (Fig. 1a). A similar trend is also observed in C-rate cycling, as seen in Fig. 1b and summarized in Table S2. The capacity provided by HSC25 (35 mAh g^{-1}) at 1000 mA g^{-1} current density is 2.3-fold increased in HSC75 (80 mAh g^{-1}). On the contrary, HSC25 performs far better in long-term cycling at 100 mA g^{-1} current density. Capacity retention at the end of 100th cycle with respect to initial capacity for HSC25, HSC50, and HSC75 is 89.2%, 79.7%, and 70.2%, respectively (Fig. 1c). Similarly, the trend of average coulombic efficiency throughout 100 cycles runs as: HSC25 (89.7%) > HSC50 (78.2%) > HSC75 (75.6%) as shown in Fig 1d. The higher surface area of HSC helps in increasing the capacity but is also the reason behind the poor cycling efficiency. It catalyzes the electrolyte decomposition at higher voltages. The 5.00 V peak during charge in differential capacity profile (Fig. S2a) is most intense in HSC75. The less-intense counter redox peak at discharge indicates that it originates from electrolyte decomposition. As a result, the reversibility is hampered by increasing the percentage of HSC in the composition.

All the composite materials exhibit lower efficiencies for a few initial cycles (Fig. 1d). This phenomenon is very common in the case of anion storage [22]. It is caused by the reorganization of graphene sheets under the circumstances of anion intercalation. Anions need to overcome the cohesive Van der Waals force between two graphene layers to position themselves at particular lattice sites of graphite [35]. It requires an energy equivalent to a voltage of 4.55 V for bulkier anions (76 pm ionic radius of Li^+ vs. 350 × 350 pm^2 area of PF_6^-) to intercalate. After the initial accommodation of anions, graphene sheets undergo self-reorganization to widen the edge sites allowing easier intercalation of anions in the subsequent cycles. It is reflected in the shift of onset potential for anion intercalation from 4.55 V at the 1st cycle to 4.52 V at 20th cycle. The 30 mV shift towards lower voltage not only eases intercalation but also widens the voltage range of intercalation that may allow more anions into the host. Anions intercalated in the first few cycles are irreversibly trapped to exert pillar effect on graphite that resists the host structure from crumbling down and results in lower coulombic efficiency. It is also reflected in the initial irreversible expansion of graphite, as revealed by the electrochemical dilatometry study [36]. The overall expansion of electrode dimensions is relatively

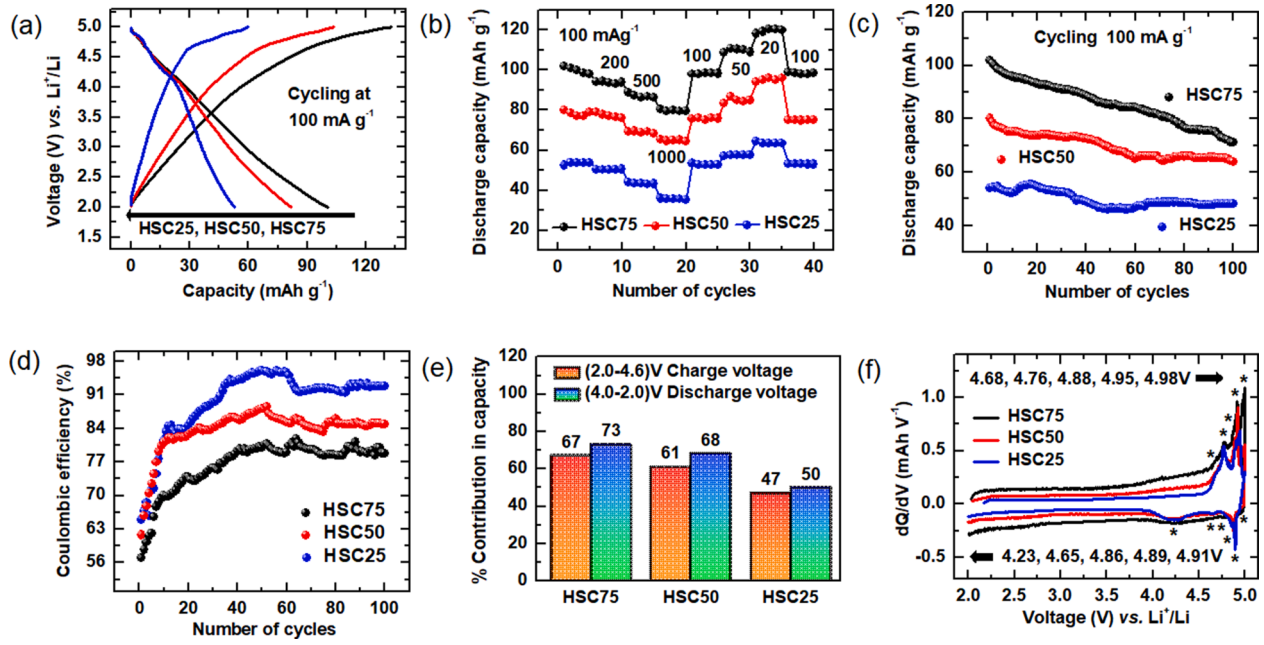

Fig. 1. Comparison plots of graphite-HSC composites at three different ratios (HSC75, HSC50, and HSC25) against lithium metal anode within 2.0–5.0 V range using 1 M $LiPF_6$ in 1:1 ratio of EC-DEC electrolyte. (a) First cycle voltage profiles for charge-discharge cycling at 100 mA g^{-1} current density, (b) C-rate performance studies for 5 cycles each at current densities of 100, 200, 500, 1000, 100, 50, 20, and 100 mA g^{-1}, respectively. Long-term cycling at 100 mA g^{-1} current density until 30% fade with respect to initial capacity: (c) discharge capacity vs. cycle number plots, and (d) coulombic efficiency vs. cycle number plots, (e) Bar diagram for the percentage of capacity obtained in (2.0–4.6) V range during charge and (4.0–2.0) V range during discharge i.e., surface contribution at 100 mA g^{-1} cycling, and (f) Differential capacity plots for 100 mA g^{-1} cycling.

higher during first few cycles. This reorganization effect is much more pronounced for anions bulkier than PF_6^- ($TFSI^-$, $FTFSI^-$, $BETI^-$, etc.). As an outcome, the capacity fading curve of anion intercalation is little steeper initially than the rest of the cycles. Although in composite materials, apart from the reorganization effect, electrolyte decomposition on the surface of non-graphitic carbon and delay in electrolyte penetration for thicker electrodes also play auxiliary roles.

The capacities in the range of 2.0–4.5 V and 4.0–2.0 V during charge and discharge, respectively, are contributed via the surface storage mechanism. The percentage of capacity incurred in this range compared to overall capacity (2.0–5.0 V of charge and 5.0–2.0 V of discharge) increases with the weight percent of HSC in the composite due to its high surface area, as illustrated in Fig. 1e. Surface and intercalation capacities in both charge and discharge processes are well-balanced, i.e., around 50±3% for HSC25 (Table 1). One point to note here is that surface contribution in discharge capacity is higher than charge capacity irrespective of the wt.% of HSC in the composite. Underestimation of surface effects in 4.9–5.0 V during charge, where electrolyte decomposition comes into effect, is one of the valid reasons. Another reason may be assigned to the extended voltage range of deintercalation (5.0–4.0 V) compared to intercalation (4.5–5.0 V). Delay in deintercalation by 400–500 mV is a common phenomenon in the case of anion storage within carbonaceous materials. Bulkier anions exert a strong repulsive force on each other in the overcrowded environment inside the host structure at the end of the charge. It impedes the ionic mobility of anions along the two-dimensional diffusional pathway of graphite structure.

Table 1
Percentage of intercalation and surface contribution to capacity.

Materials	% Contribution to capacity @ 100 mA g^{-1}			
	Charge		Discharge	
	% Surface	% Intercalation	% Surface	% Intercalation
HSC75	67	33	73	27
HSC50	61	39	68	32
HSC25	47	53	50	50

Due to the sluggish kinetics, large polarization occurs between the charge and discharge processes. Differential capacity plots also exhibit the same behavior (Fig. 1f). All the composites demonstrate 5 sets of peaks similar to graphite (Fig. S1d). The only difference is the gradual flattening of discharge peaks with increased wt.% of non-graphitic carbon in the composite due to enhanced irreversibility.

In summary, the addition of non-graphitic carbon in graphite increases the anion storing capacity of carbon cathodes with the aid of surface storage mechanism. The increment is directly proportional to the weight percentage of non-graphitic carbon in the composite. Experimentally obtained capacities from HSC75, HSC50, and HSC25 are approximately 4, 3, and 2 times higher than pristine graphite, respectively. The capacity increment factor is even larger at higher current densities. However, non-graphitic carbon introduces irreversibility issues into the system as a more exposed surface induces greater electrolyte degradation. The electrolyte decomposition irreversibly consumes anions from its limited reservoir resulting in rapid capacity decay, and the decomposition products accumulate onto the surface in thick layers to hinder the intercalation. This is the reason behind the better electrochemical performances of HSC25 than HSC50 and HSC75. Moreover, the contribution from surface storage and intercalation mechanism in obtaining capacity is evenly distributed in HSC25. Therefore, the long-term cycling stability and efficiency of HSC25 are far superior to the other two. Additional drawbacks of HSC50 and HSC75 include inferior coulombic efficiency (<80%), difficulty in loading > 5 mg cm^{-2} of active mass, and the peel-off tendency of coated material from current collectors. Only HSC25 survives up to 625 cycles (~ 25 days) before 30% capacity loss. But HSC75 and HSC50 can only withstand 100 and 168 cycles under similar testing conditions, which is not up to the practical standards (Fig. S3). A similar study with other non-graphitic carbons such as GO (Fig. S4), rGO (Fig. S5), and BNC (Fig. S6 and Table S3) having different sets of physical characteristics (Table S4) reestablishes the same trade-off between higher capacity and longer cycle life, although each non-graphitic carbon uniquely affects the surface storage phenomenon (optimization 2). Hence, further

optimizations are carried out using the 75:25 ratio of graphitic and non-graphitic carbon.

3.2. Optimization 2: type of non-graphitic carbons

Physical properties of non-graphitic carbon influence the electrochemical performances of composite cathodes. This section deals with the optimization for the type of non-graphitic carbons. GO, rGO, HSC, and BNC are chosen and mixed with graphite in a 25:75 ratio as deduced from optimization 1. The composites are hereby termed as GO25, rGO25, HSC25, and BNC25, respectively.

The powder XRD pattern proves the formation of the composite as characteristic peaks of both graphitic and non-graphitic carbons are visible (Figs. 2a and S7). Raman spectroscopy of carbonaceous materials shows two major peaks. The in-plane vibration of carbon atoms appears as Graphitic or G-band at ~ 1585 cm^{-1} with E_{2g} symmetry. The D-band located at ~ 1350 cm^{-1} arises from the defects and dislocations of carbon lattice (Fig. S8) [37]. In the studied composites, the peak positions of D and G bands are not subjected to any shift in terms of wavenumber (cm^{-1}), but the relative intensity is altered. The structural disorderedness (I_D/I_G) and degree of graphitization (DoG) (I_G / I_G+I_D) of composites are calculated from the spectrum (Fig. 2b). Previous literature reports suggest that anion intercalation is directly proportional to DoG [38]. However, the extent of increase in anion intercalation capacity is not so remarkable when DoG surpasses a value of 95% [28]. All the composite samples possess DoG values >95%. It suggests that the loss in graphitization degree as a result of compositing does not influence electrochemical properties. The difference in electrochemical performance originates solely from non-graphitic part.

Table S2 summarizes the C-rate performance of all composites, and voltage profiles are shown in Fig. S9. The capacity trend for composite cathodes is dominated by the surface area of non-graphitic carbons. BET profiles and data are shown in Figs. 2c and S10. HSC, rGO, GO, BNC and pristine graphite show BET surface areas of 2478, 235, 64, 193, and 2 $m^2 g^{-1}$, respectively. Discharge capacities shown by HSC25, rGO25, GO25, BNC25, and graphite are 55, 48, 43, 25, and 27 mAh g^{-1}, respectively, at 100 mA g^{-1} current density (Fig. 3a). HSC25 shows maximum capacity due to the highest surface area of HSC among all non-graphitic carbons. Capacity increment for HSC25 is 97% at 100 mA g^{-1} and 170% at 1000 mA g^{-1} with respect to pristine graphite (Table S2). Surprisingly, BNC25 demonstrates no improvement in capacity at any current density. It reveals that other than the surface area, doped heteroatoms and surface functional groups also influence the electrochemical properties of the composites. Charge and discharge capacities in the pre-intercalation region (2.0–4.5 V) and post-deintercalation region (4.0–2.0 V), respectively, are dominated by surface effects. HSC having the highest surface area demonstrates a maximum percentage of surface storage among all composites. In contrast, the surface contribution in GO25 overshadowed rGO25 due to the presence of relatively higher percentage of oxygen in GO than in rGO (Fig. 3b). The percentage of oxygen content in the pristine states of HSC, rGO, GO, and graphite is 4.7, 11.2, 22.2, and 2.5, respectively, whereas 2.8% N and 1.2% B are present in BNC along with 11.6% oxygen (Figs. S11 and S12, and Table S4). Effects exerted by B and N may be responsible for the poor electrochemical performance of BNC25. There exist contradictory reports in the literature on the role of heteroatoms on anion storage. Some studies suggest that heteroatoms facilitate surface adsorption-desorption kinetics of the anion, while a report revealed that N-doping not only hinders intercalation but also acts as a catalyst toward Cl_2 gas evolution from $AlCl_4^-$ anion intercalated inside graphite for Aluminium-ion battery [39,40]. Although the exact role of heteroatoms is still a question of debate, our observation indicates that functional groups improve the surface contribution by chemisorption, but the doped boron atoms (Lewis acidic center) immobilize the PF_6^- (Lewis basic group) anions via strong lewis acid – lewis base interaction. A similar interaction is also evident in electrolytes with boron-based additives and anion receptors [41]. However, detailed theoretical studies are required to unravel atomistic insights of interaction which is out of the scope. That is why no quantifiable effect of adding BNC into graphite is found, rather, the obtained capacity of the composite is lower than the pristine

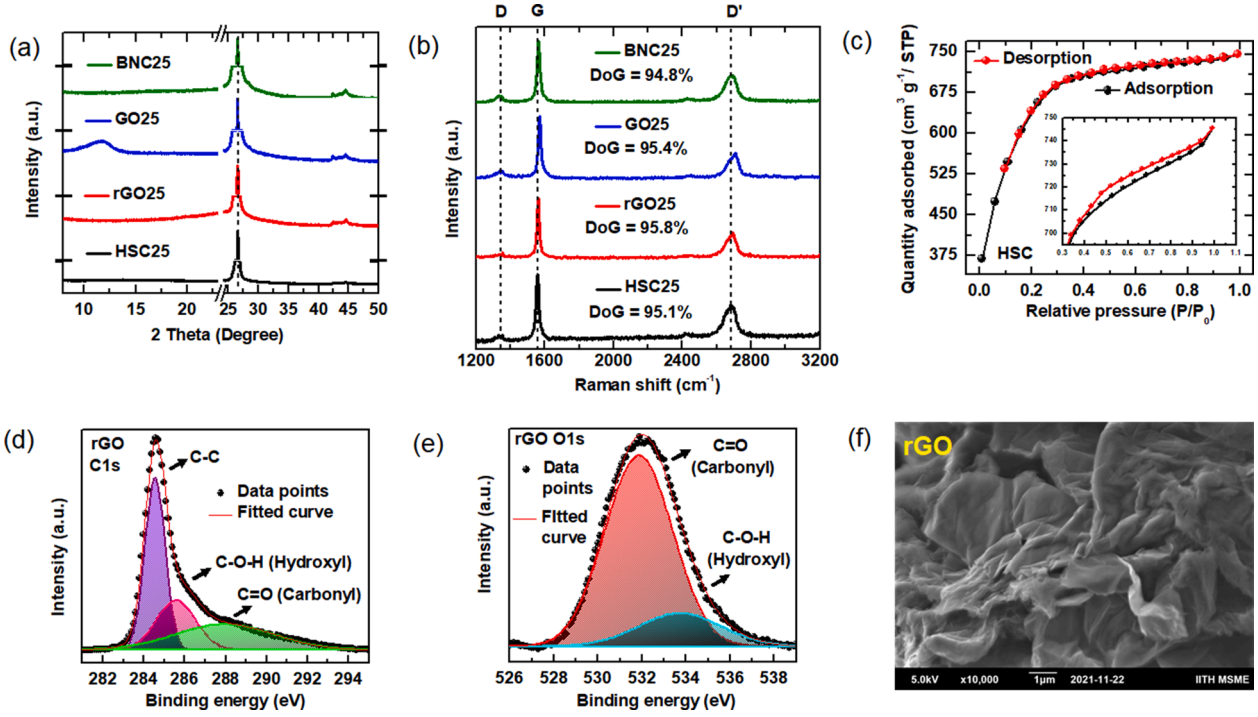

Fig. 2. Physical characterization plots of non-graphitic carbons and their composite with graphite (HSC25, rGO25, GO25, and BNC25). (a) Powder X-ray diffraction diagram of composites, (b) Raman spectrum of composites, (c) BET adsorption curve of pristine HSC. X-ray photoelectron spectra of pristine rGO. (d) C1s and (e) O1s, and (f) Scanning electron microscopy image of pristine rGO.

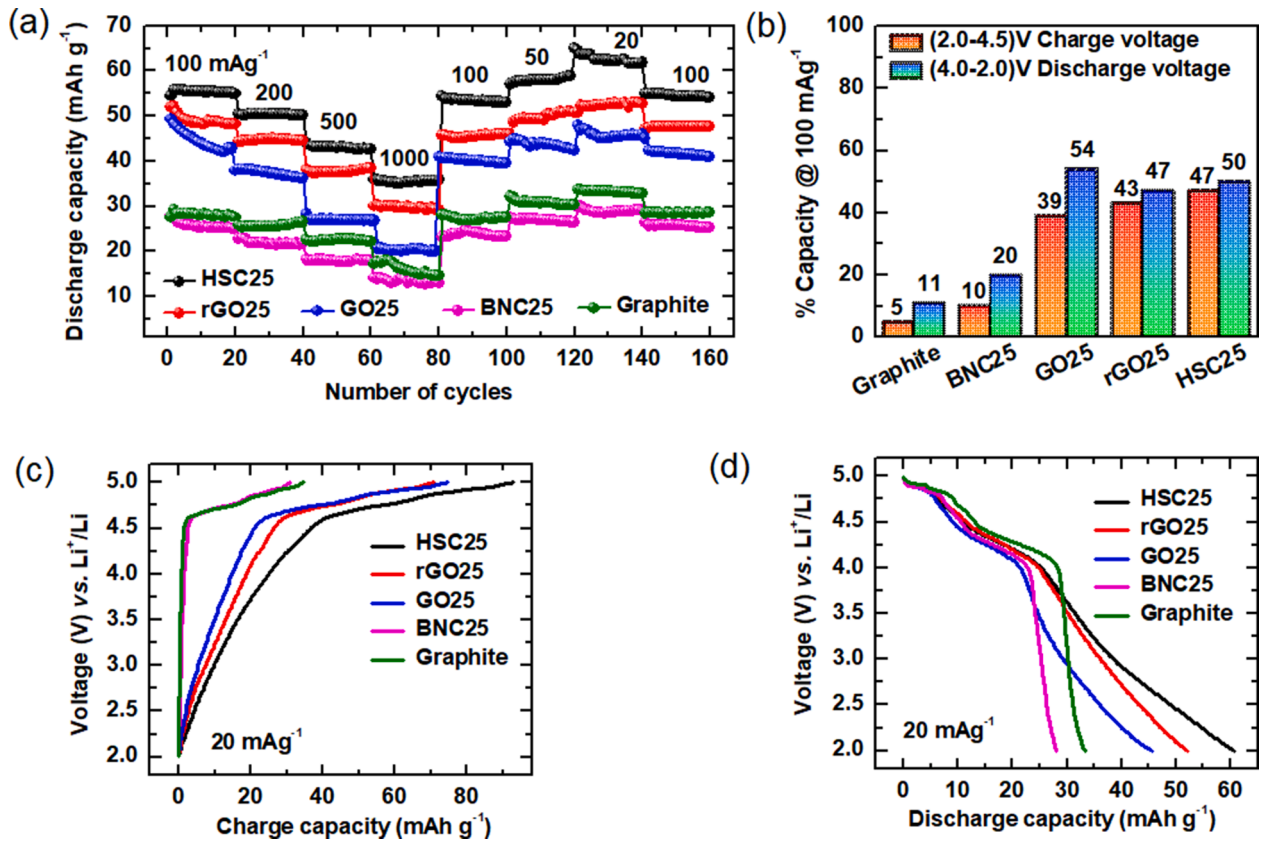

Fig. 3. Electrochemical comparison plots of 4 composites (HSC25, rGO25, GO25, and BNC 25) and pristine graphite against lithium metal anode within 2.0–5.0 V range using 1 M $LiPF_6$ in 1:1 ratio of EC-DEC electrolyte. (a) C-rate performance studies. 20 cycles each at current densities of 100, 200, 500, 1000, 100, 50, 20, and 100 mA g^{-1}, respectively, (b) Bar diagram for percentage of capacity obtained in (2.0–4.5) V range during charge and (4.0–2.0) V range during discharge, i.e., surface contribution for cycling at 20 mA g^{-1} current density, (c) Charge profiles, and (d) discharge profiles of composites at 20 mA g^{-1} current density.

graphite due to the mentioned interaction. Coulombic efficiency of BNC25 takes more than 50 cycles to reach a stable value above 90%, whereas it is only 10–15 cycles for other composite samples. Although BNC25 shows similar redox behavior like other composites according to differential capacity profile (Fig. S13), onset potential of anion intercalation is affected by the presence of surface groups and doped elements as demonstrated in Table 2. It is shifted from 4.55 V of graphite to 4.58 V, 4.58 V, 4.59 V, and 4.61 V in HSC25, rGO25, GO25, and BNC25, respectively, at 20 mA g^{-1} cycling (Fig. 3c and d). The shift of 30–40 mV in HSC25, rGO25, and GO25 is caused by the surface oxygen functionalities, which creates a larger concentration gradient of anions near the electrochemically active surface and disrupts the diffusion flux of anions into the electrode. Higher current densities ($\geq$ 1000 mA g^{-1}) during fast cycling worsen the situation by delaying the intercalation further by $\geq$ 200 mV (Fig. S14). Consequently, the endpoint of deintercalation also undergoes a lower voltage shift (from 4 V vs. Li^+/Li of graphite to 3.9 V at 100 mA g^{-1} and 3.5 V at 1000 mA g^{-1}). Moreover, the presence of B and N ensued the 20–25 mV of additional delay during both charge and discharge for BNC25, referring to the negative impacts of B and N on anion intercalation. Figs. 2f and S15 represent SEM images of rGO and other non-graphitic carbons. Graphite possesses a near-spherical morphology with micrometer sized secondary particles. rGO and GO show nanosheet type morphology, while HSC and BNC are irregularly shaped. Nevertheless, no strong correlation between morphology and capacity improvement is found.

Table 2
Onset potential of anion intercalation at different current densities.

Onset potential vs. Li^+/Li		*Current density (mA g^{-1})*		
		20	100	1000
Materials	HSC25	4.58	4.61	4.78
	rGO25	4.58	4.61	4.78
	GO25	4.59	4.62	4.79
	BNC25	4.61	4.64	4.80
	Graphite	4.55	4.58	4.78

Mechanism of anion storage in non-graphitic carbons is an unresolved problem in the field. This section qualitatively discusses the mechanistic pathways of anion storage and why it is not so effective as cation storage. The explanation is as follows – a) Ions can form multilayers in tilted and randomly cluttered graphene sheets of non-graphitic carbons. This route is responsible for cation storage in hard and soft carbons [42]. But the long-range graphitic order is an essential criterion for anionic accumulation. Even the slightest disorder interrupts the build-up of extended layers of anions and diminishes the capacity to a lower value. Hence, turbostratically disordered carbons are not an efficient host of anions. b) Surface functional groups and doped heteroatoms contribute towards capacity for both cations and anions by chemisorption [43]. However, the interplay between such functionalities and anions is not clearly understood. c) Cavities in the structure also render the space for both cations and anions [44]. A uniformly distributed network of hierarchical pores is most effective for this purpose. Macropores (>50 nm) facilitate the ionic penetration and shorten the diffusion pathlength, mesopores (2–50 nm) provide the transport passage for ions to pass through, and the micropores (< 2 nm) offer the active sites for ion storage [45]. d) One of the most capacity contributing factors for cations is cluster formation. In-situ formation of metallic

nanoclusters during electrochemical cycling imparts a valuable percentage of overall capacity [46–48]. Counter-anion of electrolyte salt (PF_6^- here) being a negatively charged species is incapable of doing so. Therefore, cluster formation is not a feasible option for anion storage. In short, pseudocapacitive mechanisms are not so potent for storing anions compared to cation storage. Eventually, a non-graphitic host alone turns out to be less advantageous in terms of capacity than graphitic carbon. However, blending both the material in a suitable ratio is susceptible towards capacity improvement, as evident in optimization 2.

In summary, compositing 25% HSC with 75% of graphite almost doubles the capacity of pristine graphite at all current densities due to the high surface area of HSC. Capacity acquired from rGO25 is very close to HSC25 in spite of the much lesser surface area of rGO than HSC. It infers that chemisorption induced by surface functional groups plays a vital role here. Then again, doped heteroatoms, especially lewis acidic centers like boron, may exert a negative impact on anion storage, as shown by BNC25, but the speculation requires more clarifications from theoretical evidence. HSC25 and rGO25 are taken forward for further optimizations.

3.3. Optimization 3: long-term cycling

The cycle life of an electrochemical energy storage device is an important parameter to measure. Composites of HSC-graphite and rGO-graphite (finalized from optimization 2) in 25:75 ratio (taken from optimization 1) are subjected to galvanostatic charge-discharge cycling at different current densities until it loses 30% capacity with respect to the initial value.

HSC25 shows the highest capacity at all current densities. The surface area significantly influences anion storing performance. It not only boosts the capacity but also enhances the reactivity of electrolyte at cathode electrolyte interphase leading to the reduction in coulombic efficiency (CE). The word 'coulombic efficiency' connotes different senses in the context of LIBs and DIBs. Classically, it is defined as the ratio of (amount of Li^+ reverts to cathode) / (amount of Li^+ releasing from cathode), as the cathode is the only reservoir of lithium in LIBs (Eq. (1)). But DIBs, working on the principle of cation and anion storage, an additional term of anionic efficiency gets added up with cationic efficiency as mentioned in Eq. (2).

$$CE_{LIB} = \frac{\text{Amount of } Li^+ \text{ reverts to cathode from anode}}{\text{Amount of } Li^+ \text{ releasing from the cathode to the anode}} \quad (1)$$

$$CE_{DIB} = CE_{cation} + CE_{anion} = \frac{\text{Amount of } Li^+ \text{ reverts to electrolyte from the anode}}{\text{Amount of } Li^+ \text{ releasing from electrolyte to anode}} + \frac{\text{Amount of } PF_6^- \text{ reverts to electrolyte from the cathode}}{\text{Amount of } PF_6^- \text{ releasing from electrolyte to cathode}} \quad (2)$$

$$(\text{Capacity retention})_{LIB} = (CE)^n \quad (3)$$

Capacity retention is related to CE according to Eq. (3). This correlation is inappropriate in the case of Lithium metal batteries (LMBs) and LIB half cells as the lost Li^+ gets quickly replenished from the infinite pool of lithium. Hence, CE does not reflect the loss of lithium inventory with the progress of cycling for LMBs and LIB half cells [49]. In contrast, Li|Carbon cell studied in this work functions on a dual ion storing mechanism. It contains infinite lithium, but the amount of anion is finite. Therefore, useful information can be extracted regarding the loss of anion inventory. CE of such cell represents independent CE_{anion} value, i.e., anionic efficiency isolated from cationic efficiency (Equation ii). However, it is noteworthy to mention here that in a dual ion cell fabricated by using carbon at both sides (dual carbon cell), CE_{DIB} is not just the mere addition of two terms. The interplay between cationic and anionic efficiency weights down the overall value below the expected range.

In DIBs, CE_{cation} rises to > 99.5% after initial formation cycles, likewise LIBs. But the bigger size of anion and high voltage operation make CE_{anion} a limiting factor. It hardly crosses 99% value for cycling at standard current rates of C/2, C/5, etc. Further, CE_{anion} decreases in DIBs with the decrease in current densities, i.e., during slower rate cycling. The stability of conventional carbonate electrolytes is sacrificed at the 5 V range. The longer time the system resides at high voltage, the greater is the decomposition. Thus, the factor corresponding to the 'time spent at high voltage' overrides other parameters as a source of inefficiency. That is why CE_{avg} value is ≥ 99% at ≥ 1000 mA g^{-1} current density but ≤ 90% at ≤ 50 mA g^{-1} for composite materials, as seen in Table 4. In addition, the more exposed surface triggers the parasitic reactions at the interphase, forcing HSC25 to cycle with lower efficiency than other materials having lower surface area. The accumulated irreversible capacity value calculated according to Eqs. (4) and (5) over 622 cycles piles up to 2638 mAh g^{-1} at 100 mA g^{-1} cycling for HSC25, which is 3 times higher than rGO25 (902 mAh g^{-1}) as shown in Fig. 4c. Irreversible capacity value accumulated over a particular number of cycles gives the information about the quantity of charge carriers (anion here; as lithium metal anoderepresents an infinite source of Li^+) irreversibly trapped. It affects the cycle life of the cell.

$$\text{Irreversible capacity} = [\text{Charge capacity} - \text{Discharge capacity}] \text{ mAh } g^{-1} \quad (4)$$

$$\text{Accumulated irreversible capacity} = \sum_{n=1}^{n=622} [\text{Irrversible capacity (n)}] \text{ mAh } g^{-1} \quad (5)$$

Table 3, Figs. 4a, b, and S16, S17 report long-term galvanostatic charge-discharge cycling performances at 50, 100, 200, 500, and 1000 mA g^{-1} current densities until 30% capacity fade. rGO25 having a lower surface area performs far better than HSC25 at low current densities, and cycle life is improved. It yields a cycle life of ~ 50 days (~ 1400 cycles) until 70% capacity retention with an initial capacity of ~50 mAh g^{-1} and reaches a CE_{avg} value of 96.5% at 100 mA g^{-1} current density, as demonstrated in Fig. 4a and b. However, HSC25 shows an initial discharge capacity of 55 mAh g^{-1} (5 mAh g^{-1} more than rGO25), but the cycle life is shortened to 625 cycles (24 days) with an average coulombic efficiency of only 91.8% (4.7% lesser than rGO25). rGO25 can cycle even up to 100 days at 20 mA g^{-1} current density (Fig. S18), while HSC25 cannot perform up to the mark. Therefore, a more exposed surface of HSC aids surface anion storage but also catalyzes electrolyte decomposition. On the other hand, rGO25 having less surface area cycles much longer time at lower current densities. Besides, the lifetime gap between rGO25 and HSC25 reduces at high current densities as faster charge-discharge does not allow the system to reside much time at higher voltages. At 1000 mA g^{-1} current density, HSC25 (35 mAh g^{-1}) shows higher capacity than rGO25 (30 mAh g^{-1}) but equal lifetime (~ 8 1/2 days). It is worth mentioning that CE values and an overall lifetime can be improved by using high-voltage additives, employing pre-formed interphase, smoothening the surface by coating, etc. This optimization is devoted to bring out the relative efficacy of different composite materials in terms of electrochemical cycling and do not intend to establish a standard CE value. CE improvement can be studied separately elsewhere. The voltage efficiency and hysteresis are other two important criteria for performance comparison that are often overlooked. The dissimilarity between average charge and discharge voltage appears from the fact that higher energy is needed to activate a chemical reaction during the charging process. Further, the possibility of electrolyte decomposition at the upper charge cut-off voltage broadens the voltage gap. rGO25 achieves a voltage efficiency of 88.2% which is translated to an energy efficiency of 85.5% (Fig. 4d and e) compared to voltage efficiency and energy efficiency of 85.3 and 78.9%, respectively for HSC25. The cell-level energy efficiency of commercial Lithium-ion systems is 98–99% depending on the applied current density. The

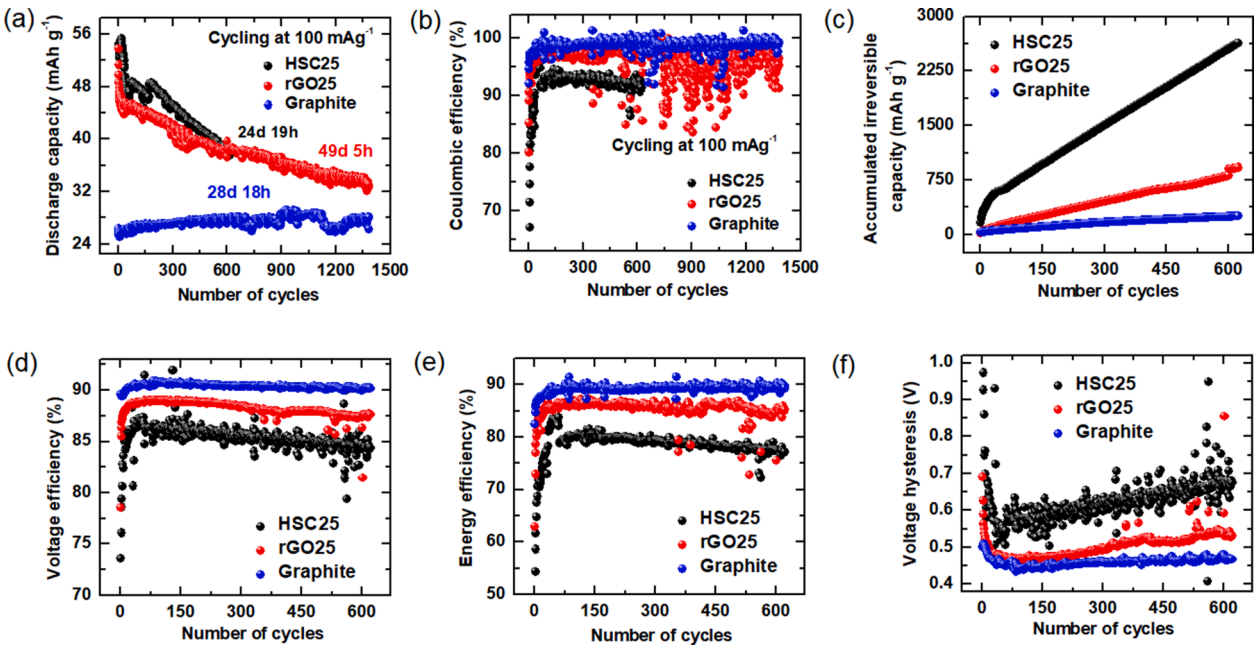

Fig. 4. Comparison plots of HSC25, rGO25, and graphite cycled against lithium metal anode within 2.0–5.0 V range using 1 M $LiPF_6$ in 1:1 ratio of EC-DEC electrolyte at 100 mA g^{-1} current density until 30% capacity fade with respect to first cycle. (a) Discharge capacity, (b) coulombic efficiency, (c) accumulated irreversible capacity, (d) voltage efficiency, (e) energy efficiency, and (f) voltage hysteresis vs. number of cycles.

Table 3
Summary of long-term cycling performances at different current densities.

Applied current density (mA g^{-1})	Materials	No. of cycles till 70% retention	Range of discharge capacity[#] (mAh g^{-1})	Total running time[^]	Achievable C-rate	Average coulombic efficiency (%)
50	HSC25	407	59–41	42d 1h	1–1.5C	78.0
	rGO25	656	51–36	64d 17h	1C	89.2
	Graphite[*]	656	30–27	23d 19h	2C	94.1
100	HSC25	625	55–38	24d 19h	2C	91.8
	rGO25	1385	49–34	49d 5h	2C	96.5
	Graphite[*]	1385	27–25	28d 18h	4C	98.7
200	HSC25	771	51–36	17d 11h	4C	93.2
	rGO25	1280	45–31	21d 19h	4C	97.1
	Graphite[*]	1280	25–21	12d 13h	9C	99.0
500	HSC25	2579	43–30	18d 20h	12C	98.3
	rGO25	3013	37–26	16d 15h	15C	98.9
	Graphite	1688	20–14	4d 9h	30C	99.3
1000	HSC25	2631	35–24	8d 18h	25C	98.8
	rGO25	3019	30–21	8d 15h	30C	99.5
	Graphite	3019	13–10	2d 20h	100C	99.5

[*] refers to < 2% capacity fade for graphite at that current density. Hence, numbers of cycles equivalent to 30% fade of rGO25 are taken for comparison.
[#] For the range of discharge capacity calculation, the initial few cycles where capacity degrade faster are excluded.
[^] Total running time refers to continuous cycling with no rest in between.

hysteresis between charge and discharge attains average values of 501 mV for rGO25, 621 mV for HSC25, whereas it is ≤ 100 mV for commercial Lithium-ion cells (Fig. 4f). Large potential hysteresis observed in DIBs stems from the electrolyte effect. The ion-pair formation, stronger attractive force between counter-ions of electrolyte salt, and tightly bound solvation sheath enlarge the overpotential gap between anion insertion and deinsertion. The polarization associated with lithium plating-stripping further accompanies the potential hysteresis. Hence, inefficiency emerging from the voltage difference showcases a more pronounced effect than CE. All voltage efficiency and hysteresis values are summarized in Table 4.

Composite cathodes outperform pristine graphite at higher current densities. HSC25 and rGO25 retains ~ 60% capacity at 25C and 30C

Table 4
Various efficiencies for long-term cycling at 100 mA g^{-1} current density.

Materials	Average coulombic efficiency (%)	Average voltage efficiency (%)	Average energy efficiency (%)	Average voltage hysteresis (mV)	Accumulated coulombic inefficiency (%)
HSC25	92.33	85.39	78.95	621	2638
rGO25	96.93	88.23	85.53	501	921
Graphite	98.72	90.37	89.22	459	253

rate, respectively (1000 mA g^{-1} current density), compared to 1C rate (50 mA g^{-1}), but the retention is only 40% in the case of graphite. HSC25 shows 35 mAh g^{-1} capacity at a high current density of 1000 mA g^{-1} which is still 7–8 mAh g^{-1} higher than what can be obtained from graphite (27–28 mAh g^{-1}) at a low current density of 100 mA g^{-1}. The achievable C-rate at corresponding current densities is twice for graphite than for composites (Table 3). The reason can be ascribed to the longer dwell time of composites on surface-capacity dominated voltage region (2.0–4.5 V during charge and 4.0–2.0 V during discharge) than graphite. The superior power performance demands more attention and is elaborately discussed in optimization 4.

In summary, rGO25 exhibits a longer lifetime with greater numbers of cycles and higher efficiency values than HSC25. From a qualitative view, surface porosity, i.e., larger numbers of micropores present in HSC contribute more towards inefficiency than surface functional groups of rGO. Porosity affects reversibility more than surface functional groups. Although quantification needs further investigations. In our experiments, ~99% CE value for composites is achieved only at >12C rate. Therefore, a hierarchical porous design with suppressed surface area and optimum surface functionalities can trade-off higher capacity against cycling efficiencies.

3.4. Optimization 4: active material loading

Ion intercalation into graphite can be divided into 4 steps – a) diffusion of solvated ions towards the host electrode through the electrolyte, b) desolvation of ions, c) crossing electrode-electrolyte interphase (EEI) barrier, and d) diffusion of desolvated ions inside the graphite lattice [50]. Energetics of anion intercalation differ from cations. Firstly, liquid state diffusion has a negligible barrier among all steps. Secondly, desolvation and EEI crossing are termed together as interfacial charge transfer, among which desolvation is the most energy-consuming process for cation intercalation (50–70 kJ mol^{-1} for Li^+) [51]. Bulky anions undergo weaker solvation, and the kinetics of shedding smaller solvation sheath is faster. That is why the activation energy of interfacial anion transfer is only 10–30 kJ mol^{-1} [52]. Thirdly, Li^+ diffusion ($D_c^{Li^+} = 10^{-9} - 10^{-7}$ cm^2 s^{-1} into graphite) inside graphite is much faster than anions ($D_c^{PF_6^-} = 10^{-12} - 10^{-13}$ cm^2 S^{-1}) [53]. Therefore, interfacial charge transfer possesses the highest activation energy barrier for cation transfer, whereas solid-state mass transfer is the rate-limiting step for anion storage. Thicker electrodes bring additional challenges by reducing the utilization of active material. Inadequate electrolyte transport, a tortuous path for electronic and ionic percolation, weakening of mechanical integrity, etc., create more hindrances [54]. Hence, optimization 4 is dedicated to study anion storage performance at extremely high current rates with thicker electrodes and to find optimum loading for the best power yield. Electrochemical performances of HSC25 with 5, 10, 15 mg cm^{-2} loading are compared at low and high current rates.

Fig. 5a shows charge-discharge cycling performance at different current rates, and the results are summarized in Table S5. Higher capacities are obtained using thinner electrodes. The difference in capacity is more prominent at higher current rates. Discharge voltage profile in Fig. 5c shows that polarization increases drastically leading to a capacity void of ≥ 10 mAh g^{-1} between 5 and 15 mg cm^{-2} loaded electrodes at 1000 mA g^{-1} current density. At current densities below 1000 mA g^{-1}, the capacity shown by 5 mg cm^{-2} loading is only 1.2–1.5 times higher than 15 mg cm^{-2}, while the factor rises up to 5 at 5000 mA g^{-1} current density. 5, 10, 15 mg cm^{-2} active material loaded cells demonstrate average capacities of 26, 12, 4 mAh g^{-1}, respectively and retains 60, 61, 24% capacity after 6500 cycles, respectively (Fig. 5b). Pristine graphite with 15 mg cm^{-2} loading shows 6.0–6.5 mAh g^{-1} of initial capacity under similar testing conditions (Fig. S19). Hence, thicker loading undermines the capacity improvement effect of the composite. 5 mg cm^{-2}

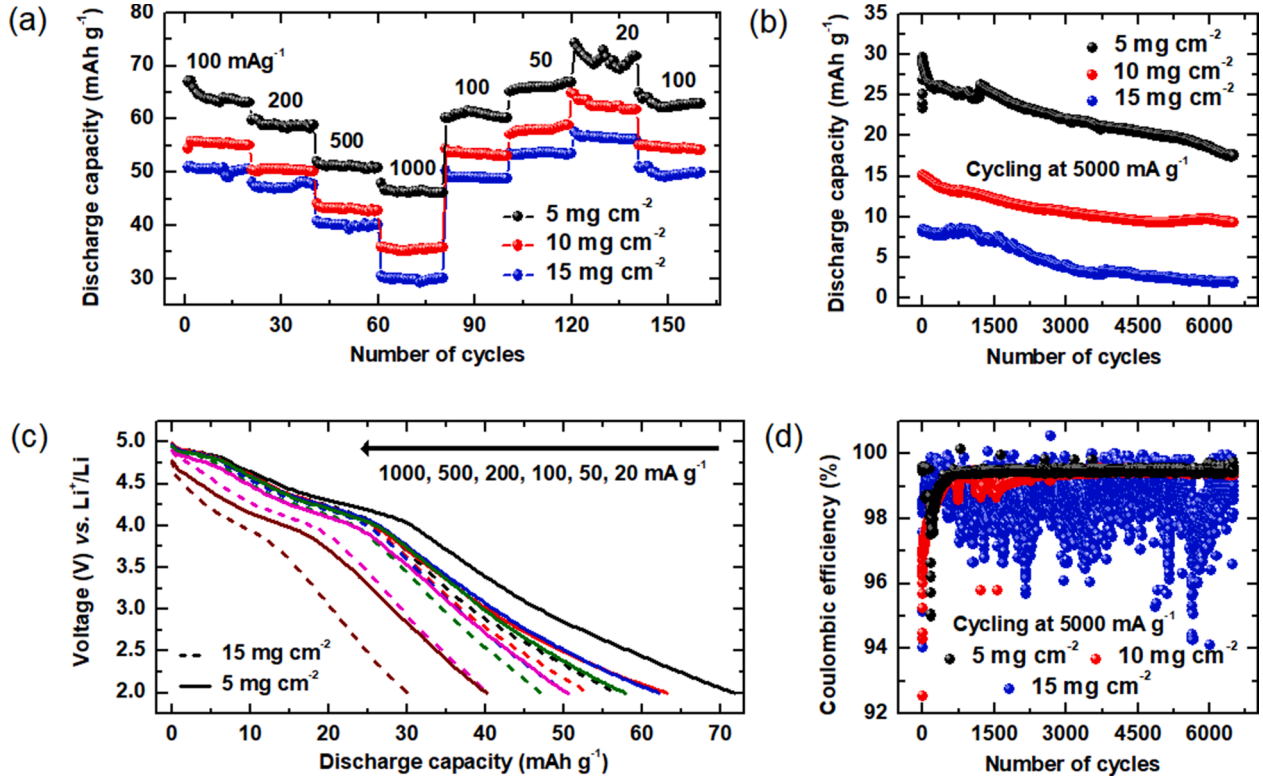

Fig. 5. Electrochemical comparison plots of HSC25 at 3 different loading densities i.e., 5, 10, and 15 mg cm^{-2} against lithium metal anode within 2.0–5.0 V range using 1 M $LiPF_6$ in 1:1 ratio of EC-DEC electrolyte. (a) Discharge capacity vs. number of cycles plot, and (c) discharge profile at 100, 200, 500, 1000, 100, 50, 20, and 100 mA g^{-1} current densities. Long-term cycling performance at 5000 mA g^{-1} current density. (b) Discharge capacity, and (d) coulombic efficiency vs. number of cycles.

loaded cell achieves a C-rate of ~ 200C at 5000 mA g^{-1} with an average coulombic efficiency of 99.5% (Fig. 5d).

In summary, solid-state mass transfer and the occurrence of additional limitations owing to high loading ($\geq$ 10 mg cm^{-2}) reduces the electrochemical performances of composite electrodes down to graphite at extremely fast cycling conditions. For example, $\leq$ 5 mg cm^{-2} loaded cell at 5000 mA g^{-1} cycling achieves a capacity value (26 mAh g^{-1}) accounting for ~ 40% with respect to 100 mA g^{-1} current density (66 mAh g^{-1}), whereas it is only 13% for 15 mg cm^{-2} loaded cell.

3.5. Dual carbon cell in coin and pouch format

Optimizations suggest that HSC25 delivers maximum improvement in capacity. Dual carbon cells in a symmetric configuration using HSC25 as cathode and anode active material are fabricated in coin and pouch type formats to validate the results further. The formation of electrode-electrolyte interphase on the cathode and anode surface immobilizes active ions. To maintain the charge neutrality of electrolyte, similar numbers of cations and anions must be trapped. Uneven degree of surface layer formation at cathode and anode initiates a domino-effect on ion loss [55,56]. Eventually, the cell cannot sustain even 50 cycles. Therefore, prelithiation is essential to compensate for lost lithium and break the chain reaction of ion loss. The lithiation potential of graphite, i.e., 0.01 V, is very close to the thermodynamic potential (0 V) for lithium metal plating. Any internal reason that causes inhomogeneous current distribution induces anode polarization. Lithium plating gets facilitated when anode potential is lowered below the 0 V. Irreversible plating consumes lithium inventory inside the full cell and raises safety concerns via the formation of lithium dendrites. Therefore, HSC25 with higher lithiation potential (~ 200 mV) is used here as the anode.

HSC25 anode is prelithiated against lithium counter electrode at 20 mA g^{-1} current density for 18 h (Fig. S22). The mass ratio of the cathode to anode is kept at 1.2:1. The dual carbon coin cell using HSC25 cathode and prelithiated HSC25 anode shows an initial capacity of 57.6 mAh g^{-1} with respect to the weight of cathode only and losses 70% of its initial capacity at the end of 415 cycles (Fig. 6a). The first cycle coulombic efficiency is 73.6%, and after the initial few cycles, it reaches an average of 92–93% like Li|Graphite cell. Other electrochemical characteristics like onset potential of anion intercalation, the evolution of voltage profile, and cell resistances except for cycle life of dual carbon coin cell remain within ± 5% compared to Li|Graphite cell. A dual carbon pouch cell is fabricated using 5 × 5 cm^2 of HSC25 cathode and prelithiated HSC25 anode. Impedance data taken after the 72 h rest period at open circuit potential demonstrates minimal values of resistances (Fig. 6b). It indicates that polarization effects do not arise from pouch fabrication issues or external connections. The voltage profile throughout the cycle does not change (Fig. 6c). The cell shows 9.5 mAh of discharge capacity (~52.7 mAh g^{-1} with respect to the weight of cathode active material) at the first cycle, which decreases to a stable value of ~ 8.2 mAh after 10 cycles, as demonstrated in Fig. 6d. These ten cycles at the beginning account for the highest amount of irreversible loss and coulombic efficiency of below 90%. This proves that the effect of compositing graphite with HSC is also visible in dual carbon cells. However, the shortening of cycle life in dual carbon cell compared with Li|Graphite cell can be attributed to the loss of active ions resulting from the anode. Lithium loss can be compensated to some extent by

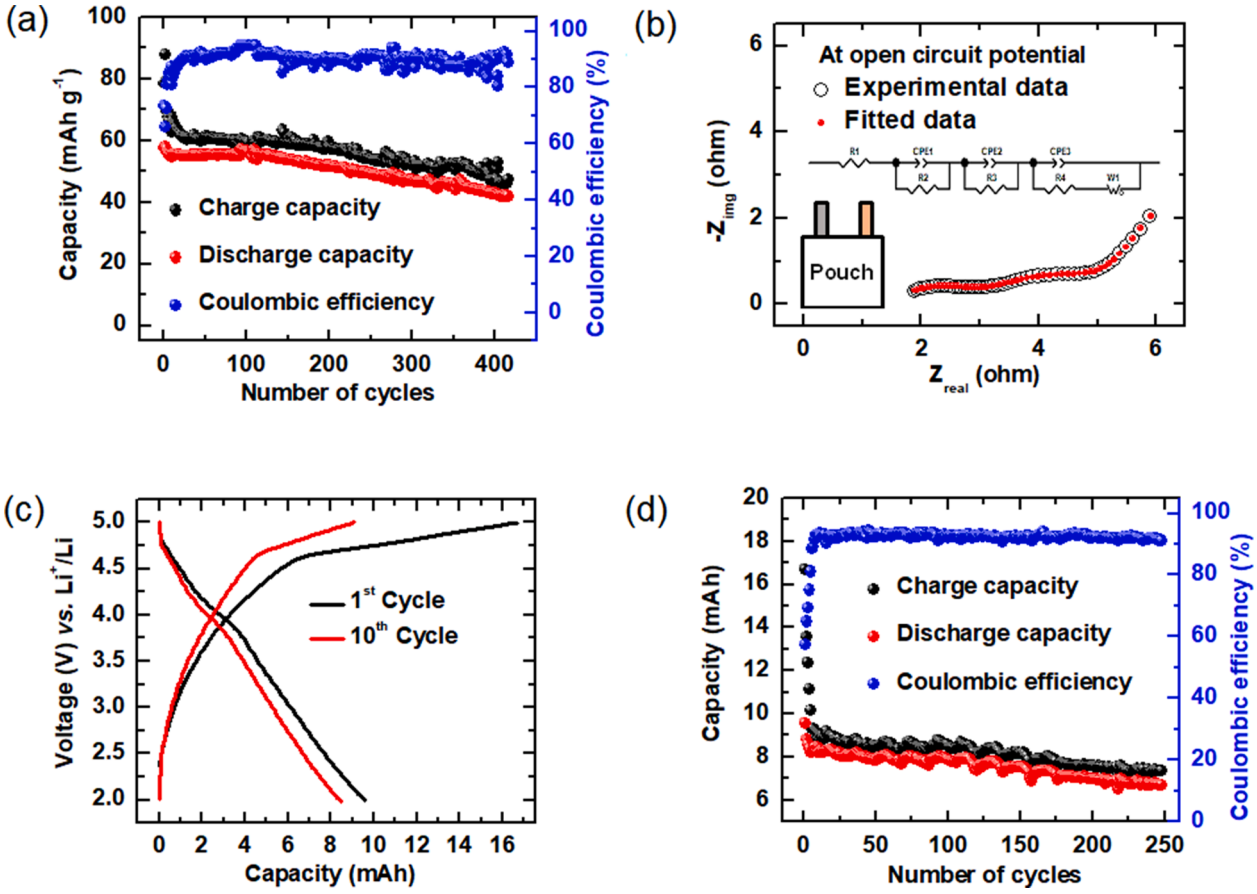

Fig. 6. (a) Capacity and coulombic efficiency vs. number of cycles plot for dual carbon coin cell using HSC25 as cathode active material and prelithiated HSC25 as anode active material (N:P ratio = 1:1.2) within 2.0–5.0 V range at 100 mA g^{-1} current density. Electrochemical performance of single stacked pouch cell using HSC25 as active material at both cathode and anode within 2.0–5.0 V range at 100 mA g^{-1} current density. (b) Electrochemical impedance spectroscopy after 72 h of fabrication, (c) 1st and 10th cycle voltage profile, and (d) capacity and coulombic efficiency vs. number of cycles plot for 250 cycles.

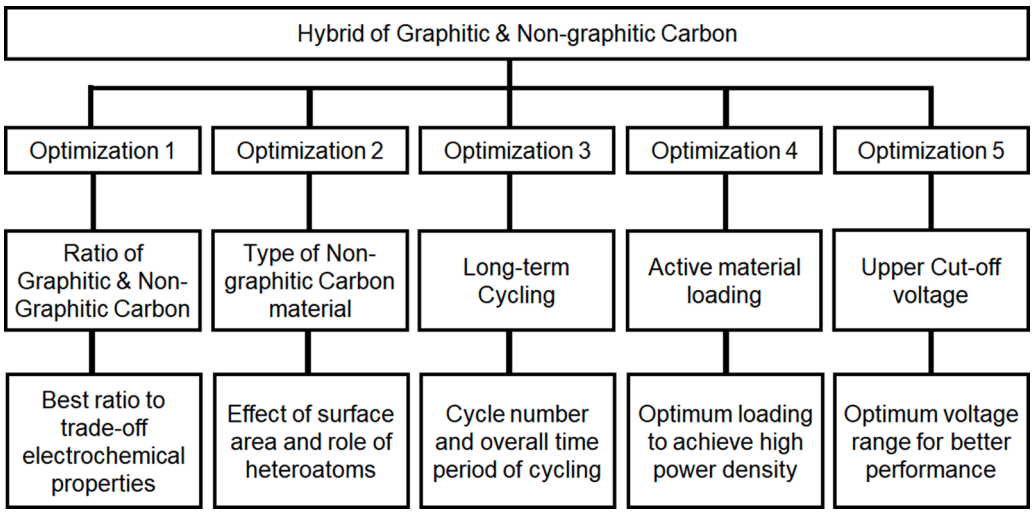

Scheme. 1. Schematic of electrochemical optimizations for graphite/ non-graphitic carbon composites studied in this work.

prelithiation but cannot be nullified completely. Moreover, lithium plating at localized regions due to the presence of 75% graphite in the anode, thicker coating, and short time of charge per cycle (a restriction insisted by cathode limitations) depletes more lithium. The irreversible lithium accommodation is accompanied by an equivalent quantity of anion trapping at the cathode to maintain charge neutrality of the electrolyte. The mutual assistance causes huge loss, as evident in the first few cycles, and affects cycle life heavily. There are several ways to mitigate anodic issues to prolong the cycle life, which is under development and will be reported in future

4. Conclusions

The limited anion storage capacity of graphite presents a severe bottleneck to dual-ion energy storage devices. The strategy to mix graphite and non-graphitic carbons to improve capacity is explored in this work through various optimizations. 75:25 ratio of graphitic and non-graphitic carbon balances intercalation and surface capacity perfectly, as revealed by optimization 1 (Ratio of graphitic to non-graphitic carbons). Optimization 2 (Type of non-graphitic carbons) and 3 (Long-term cycling) suggest that the surface area of non-graphitic materials and surface functionalities affect the capacity. HCS25 yields ~ 100% increment, whereas rGO25 is suitable for prolonged cycle life. Solid-state mass transfer limitation in the case of anion storage is further aggravated by thicker coating. $\leq$ 5 mg cm^{-2} loading brings a decent parity to energy-power output at fast cycling conditions, as shown by optimization 4 (Active material loading). However, the long-term cycling at high voltage accumulates inefficiency. Electrochemical performance severely deteriorates beyond 5 V cycling, as revealed by optimization 5 (Upper charge cut-off voltage) in Supplementary material. A schematic summary of results obtained from electrochemical optimizations is depicted in scheme S1. The results obtained in Li| Graphite cell is further validated by dual carbon cell in coin and pouch format.

Efforts to draw additional capacity make the system more prone towards enhanced degradation. As a result, coulombic efficiency is lowered, and the self-discharge rate is amplified. However, the electrochemical studies are performed using the state-of-the-art LIB electrolyte, i.e., 1 M $LiPF_6$ in 1:1 ratio of EC-DEC, which is not a commercial option for high voltage systems. Elevation in irreversibility can be tackled by using high voltage additives, F-rich artificial interphase, smooth surface coating to decrease electrolyte decomposition, etc. This work is more emphasized on the material level alterations keeping the electrolyte fixed. Overall improvement can be manifolded by using advanced electrolytes, hindering Li-plating at the anode, utilizing cellulosic separator with better electrolyte soaking property instead of glassy fiber, and ceramic-coated cell parts to deal with high voltage corrosivity, etc. Still, the extent of increment from pure graphitic to composite system will remain the same. Moreover, the strategy of compositing presented here can be extrapolated to other anion storing systems irrespective of the type of anions (BF_4^-, ClO_4^-, FSI^-, $TFSI^-$, $AlCl_4^-$, etc., instead of PF_6^-), counter cations (Na^+, K^+, Ca^{+2}, Al^{+3}, Mg^{+2}, etc., instead of Li^+), electrolyte solvent (non-aqueous solvent other than EC-DEC and aqueous media), and physical properties of graphite (surface area, particle size, pore size distribution, etc.). In addition, capacity enhancement may cause a diminution in reversibility. Therefore, other electrochemical properties should be carefully optimized to bring out the best electrochemical performance from the system.

CRediT authorship contribution statement

Shuvajit Ghosh: Conceptualization, Data curation. **Nihad MP:** . **Sadananda Muduli:** . **Subhajit Bhowmik:** . **Surendra K. Martha:** Supervision, Funding acquisition, Conceptualization.

Declaration of Competing Interest

The authors declare that they have no known competing financial interests or personal relationships that could have appeared to influence the work reported in this paper.

Data availability

Data will be made available on request.

Acknowledgments

Shuvajit Ghosh acknowledges CSIR, Govt. of India (File No. 09/1001 (0067)/2019-EMR-I), Sadananda Muduli acknowledges Ministry of Education (MoE), Govt. of India, and Subhajit Bhowmik acknowledges DST-SERB (Sanction Order: DST/TMD/MECSP/2K17/20) for fellowship. Dr. Surendra K. Martha acknowledges SERB (file no. IPA/2021/000007), Govt. of India, for financial support of the work. We thank Manajit Das, Ph.D. student at Indian Institute of Technology Bombay, India, for his help in computer coding the formulas of accumulated coulombic inefficiency and accumulated irreversible capacity. We thank China Steel Corporation, Taiwan for supplying graphite.

Supplementary materials

Supplementary material associated with this article can be found, in the online version, at doi:10.1016/j.electacta.2022.141754.

References

[1] X. Wu, K. Song, X. Zhang, N. Hu, L. Li, W. Li, L. Zhang, H. Zhang, Safety issues in lithium ion batteries: materials and cell design, Front. Energy Res. 7 (2019) 65.

[2] L. Lu, X. Han, J. Li, J. Hua, M. Ouyang, A review on the key issues for lithium-ion battery management in electric vehicles, J. Power Source. 226 (2013) 272–288, https://doi.org/10.1016/j.jpowsour.2012.10.060.

[3] Y. Chen, Y. Kang, Y. Zhao, L. Wang, J. Liu, Y. Li, Z. Liang, X. He, X. Li, N. Tavajohi, B. Li, A review of lithium-ion battery safety concerns: the issues, strategies, and testing standards, J. Energy Chem. 59 (2021) 83–99, https://doi.org/10.1016/j.jechem.2020.10.017.

[4] Y.E. Durmus, H. Zhang, F. Baakes, G. Desmaizieres, H. Hayun, L. Yang, M. Kolek, V. Küpers, J. Janek, D. Mandler, Side by side battery technologies with lithium-ion based batteries, Adv. Energy Mater. 10 (2020), 2000089.

[5] A. Manthiram, X. Yu, S. Wang, Lithium battery chemistries enabled by solid-state electrolytes, Nat. Rev. Mater. 2 (2017) 1–16.

[6] M.M. Thackeray, C. Wolverton, E.D. Isaacs, Electrical energy storage for transportation—approaching the limits of, and going beyond, lithium-ion batteries, Energy Environ. Sci. 5 (2012) 7854–7863, https://doi.org/10.1039/C2EE21892E.

[7] H.-.H. Ryu, H.H. Sun, S.-.T. Myung, C.S. Yoon, Y.-.K. Sun, Reducing cobalt from lithium-ion batteries for the electric vehicle era, Energy Environ. Sci. 14 (2021) 844–852.

[8] S.W.D. Gourley, T. Or, Z. Chen, Breaking free from cobalt reliance in lithium-ion batteries, iScience 23 (2020), 101505.

[9] K. Turcheniuk, D. Bondarev, V. Singhal, G. Yushin, Ten years left to redesign lithium-ion batteries, (2018).

[10] X. Sun, H. Hao, P. Hartmann, Z. Liu, F. Zhao, Supply risks of lithium-ion battery materials: an entire supply chain estimation, Mater. Today Energy 14 (2019), 100347.

[11] E.A. Olivetti, G. Ceder, G.G. Gaustad, X. Fu, Lithium-ion battery supply chain considerations: analysis of potential bottlenecks in critical metals, Joule 1 (2017) 229–243.

[12] T. Bartsch, F. Strauss, T. Hatsukade, A. Schiele, A.-.Y. Kim, P. Hartmann, J. Janek, T. Brezesinski, Gas evolution in all-solid-state battery cells, ACS Energy Lett. 3 (2018) 2539–2543.

[13] A.M. Bates, Y. Preger, L. Torres-Castro, K.L. Harrison, S.J. Harris, J. Hewson, Are solid-state batteries safer than lithium-ion batteries? Joule 6 (2022) 742–755, https://doi.org/10.1016/j.joule.2022.02.007.

[14] N.E. Galushkin, N.N. Yazvinskaya, D.N. Galushkin, Mechanism of gases generation during lithium-ion batteries cycling, J. Electrochem. Soc. 166 (2019) A897.

[15] S. Ghosh, U. Bhattacharjee, S. Bhowmik, D. Martha, K. Surendra, A review on high-capacity and high-voltage cathodes for next-generation lithium-ion batteries, J. Nucl. Energy Sci. Power Gener. Technol. 4 (2022), 1–1.

[16] R. Hou, B. Liu, Y. Sun, L. Liu, J. Meng, M.D. Levi, H. Ji, X. Yan, Recent advances in dual-carbon based electrochemical energy storage devices, Nano Energy 72 (2020), 104728.

[17] T. Placke, A. Heckmann, R. Schmuch, P. Meister, K. Beltrop, M. Winter, Perspective on performance, cost, and technical challenges for practical dual-ion batteries, Joule 2 (2018) 2528–2550.

[18] Q. Dou, N. Wu, H. Yuan, K.H. Shin, Y. Tang, D. Mitlin, H.S. Park, Emerging trends in anion storage materials for the capacitive and hybrid energy storage and beyond, Chem. Soc. Rev. 50 (2021) 6734–6789.

[19] X. Zhang, Y. Tang, F. Zhang, C.-.S. Lee, A novel aluminum–graphite dual-ion battery, Adv. Energy Mater. 6 (2016), 1502588.

[20] Z. Guo, Z. Xu, F. Xie, J. Feng, M. Titirici, Strategies for high energy density dual-ion batteries using carbon-based cathodes, Adv. Energy Sustainab. Res. 2 (2021), 2100074.

[21] S. Chen, Q. Kuang, H.J. Fan, Dual-carbon batteries: materials and mechanism, Small 16 (2020), 2002803.

[22] T. Placke, O. Fromm, S.F. Lux, P. Bieker, S. Rothermel, H.-.W. Meyer, S. Passerini, M. Winter, Reversible intercalation of Bis(trifluoromethanesulfonyl)imide anions from an ionic liquid electrolyte into graphite for high performance dual-ion cells, J. Electrochem. Soc. 159 (2012) A1755, https://doi.org/10.1149/2.011211jes.

[23] K. Beltrop, P. Meister, S. Klein, A. Heckmann, M. Grünebaum, H.-.D. Wiemhöfer, M. Winter, T. Placke, Does size really matter? New insights into the intercalation behavior of anions into a graphite-based positive electrode for dual-ion batteries, Electrochim. Acta 209 (2016) 44–55, https://doi.org/10.1016/j.electacta.2016.05.012.

[24] X. Jiang, L. Luo, F. Zhong, X. Feng, W. Chen, X. Ai, H. Yang, Y. Cao, Electrolytes for dual-carbon batteries, ChemElectroChem 6 (2019) 2615–2629.

[25] L. Xiang, X. Ou, X. Wang, Z. Zhou, X. Li, Y. Tang, Highly concentrated electrolyte towards enhanced energy density and cycling life of dual-ion battery, Angew. Chem. Int. Ed. 59 (2020) 17924–17930, https://doi.org/10.1002/anie.202006595.

[26] J. Li, C. Han, X. Ou, Y. Tang, Concentrated electrolyte for high-performance Ca-ion battery based on organic anode and graphite cathode, Angew. Chem. Int. Ed. 61 (2022), e202116668.

[27] A. Heckmann, J. Thienenkamp, K. Beltrop, M. Winter, G. Brunklaus, T. Placke, Towards high-performance dual-graphite batteries using highly concentrated organic electrolytes, Electrochim. Acta 260 (2018) 514–525, https://doi.org/10.1016/j.electacta.2017.12.099.

[28] A. Heckmann, O. Fromm, U. Rodehorst, P. Münster, M. Winter, T. Placke, New insights into electrochemical anion intercalation into carbonaceous materials for dual-ion batteries: impact of the graphitization degree, Carbon N Y 131 (2018) 201–212.

[29] T. Placke, S. Rothermel, O. Fromm, P. Meister, S.F. Lux, J. Huesker, H.-.W. Meyer, M. Winter, Influence of graphite characteristics on the electrochemical intercalation of bis (trifluoromethanesulfonyl) imide anions into a graphite-based cathode, J. Electrochem. Soc. 160 (2013) A1979.

[30] K. Yang, Q. Liu, Y. Zheng, H. Yin, S. Zhang, Y. Tang, Locally ordered graphitized carbon cathodes for high-capacity dual-ion batteries, Angew. Chem. Int. Ed. 60 (2021) 6326–6332.

[31] M. Wang, Y. Tang, A review on the features and progress of dual-ion batteries, Adv. Energy Mater. 8 (2018), 1703320.

[32] W.S. Hummers, R.E. Offeman, Preparation of graphitic oxide, J. Am. Chem. Soc. 80 (1958), https://doi.org/10.1021/ja01539a017, 1339–1339.

[33] P.K. Jha, S.K. Singh, V. Kumar, S. Rana, S. Kurungot, N. Ballav, High-level supercapacitive performance of chemically reduced graphene oxide, Chem. 3 (2017) 846–860, https://doi.org/10.1016/j.chempr.2017.08.011.

[34] S. Muduli, V. Naresh, S.K. Martha, Boron, nitrogen-doped porous carbon derived from biowaste orange peel as negative electrode material for lead-carbon hybrid ultracapacitors, J. Electrochem. Soc. 167 (2020), 090512.

[35] G. Schmuelling, T. Placke, R. Kloepsch, O. Fromm, H.-.W. Meyer, S. Passerini, M. Winter, X-ray diffraction studies of the electrochemical intercalation of bis (trifluoromethanesulfonyl) imide anions into graphite for dual-ion cells, J. Power Source. 239 (2013) 563–571.

[36] J.M. Huesker, M. Winter, T. Placke, Dilatometric Study of the Electrochemical Intercalation of Bis(trifluoromethanesulfonyl) imide and Hexafluorophosphate Anions into Carbon-Based Positive Electrodes, ECS Trans. 69 (2015) 9, https://doi.org/10.1149/06922.0009ecst.

[37] A.C. Ferrari, J. Robertson, Interpretation of Raman spectra of disordered and amorphous carbon, Phys. Rev. B 61 (2000) 14095.

[38] S. Ghosh, U. Bhattacharjee, S. Patchaiyappan, J. Nanda, N.J. Dudney, S.K. Martha, Multifunctional utilization of pitch-coated carbon fibers in lithium-based rechargeable batteries, Adv. Energy Mater. 11 (2021), 2100135, https://doi.org/10.1002/aenm.202100135.

[39] S. Chen, J. Wang, L. Fan, R. Ma, E. Zhang, Q. Liu, B. Lu, An ultrafast rechargeable hybrid sodium-based dual-ion capacitor based on hard carbon cathodes, Adv. Energy Mater. 8 (2018), 1800140.

[40] A.S. Childress, P. Parajuli, J. Zhu, R. Podila, A.M. Rao, A Raman spectroscopic study of graphene cathodes in high-performance aluminum ion batteries, Nano Energy 39 (2017) 69–76.

[41] E.R. Logan, J.R. Dahn, Electrolyte design for fast-charging Li-ion batteries, Trend. Chem. 2 (2020) 354–366.

[42] J.R. Dahn, T. Zheng, Y. Liu, J.S. Xue, Mechanisms for lithium insertion in carbonaceous materials, Science 270 (1995) 590–593.

[43] Y. Yuan, Z. Chen, H. Yu, X. Zhang, T. Liu, M. Xia, R. Zheng, M. Shui, J. Shu, Heteroatom-doped carbon-based materials for lithium and sodium ion batteries, Energy Storage Mater. 32 (2020) 65–90.

[44] N.A. Kaskhedikar, J. Maier, Lithium storage in carbon nanostructures, Adv. Mater. 21 (2009) 2664–2680.

[45] U. Bhattacharjee, S. Bhowmik, S. Ghosh, N. Vangapally, S.K. Martha, Boron-doped graphene anode coupled with microporous activated carbon cathode for lithium-ion ultracapacitors, Chem. Eng. J. 430 (2022), 132835, https://doi.org/10.1016/j.cej.2021.132835.

[46] Y. Youn, B. Gao, A. Kamiyama, K. Kubota, S. Komaba, Y. Tateyama, Nanometer-size Na cluster formation in micropore of hard carbon as origin of higher-capacity Na-ion battery, npj Comput. Mater. 7 (2021) 1–8.

[47] S. Alvin, H.S. Cahyadi, J. Hwang, W. Chang, S.K. Kwak, J. Kim, Revealing the intercalation mechanisms of lithium, sodium, and potassium in hard carbon, Adv. Energy Mater. 10 (2020), 2000283.

[48] L.M. Bloi, F. Hippauf, T. Boenke, M. Rauche, S. Paasch, K. Schutjajew, J. Pampel, F. Schwotzer, S. Dörfler, H. Althues, M. Oschatz, E. Brunner, S. Kaskel, Mechanistic insights into the reversible lithium storage in an open porous carbon via metal cluster formation in all solid-state batteries, Carbon N Y 188 (2022) 325–335, https://doi.org/10.1016/j.carbon.2021.11.061.

[49] J. Xiao, Q. Li, Y. Bi, M. Cai, B. Dunn, T. Glossmann, J. Liu, T. Osaka, R. Sugiura, B. Wu, Understanding and applying coulombic efficiency in lithium metal batteries, Nat. Energy 5 (2020) 561–568.

[50] K. Xu, Y. Lam, S.S. Zhang, T.R. Jow, T.B. Curtis, Solvation sheath of Li+ in nonaqueous electrolytes and its implication of graphite/electrolyte interface chemistry, J. Phys. Chem. C 111 (2007) 7411–7421.

[51] W. Cai, Y.-.X. Yao, G.-.L. Zhu, C. Yan, L.-.L. Jiang, C. He, J.-.Q. Huang, Q. Zhang, A review on energy chemistry of fast-charging anodes, Chem. Soc. Rev. 49 (2020) 3806–3833.

[52] T. Fukutsuka, F. Yamane, K. Miyazaki, T. Abe, Electrochemical intercalation of bis (fluorosulfonyl) amide anion into graphite, J. Electrochem. Soc. 163 (2015) A499.

[53] S. Miyoshi, T. Akbay, T. Kurihara, T. Fukuda, A.T. Staykov, S. Ida, T. Ishihara, Fast diffusivity of PF6–anions in graphitic carbon for a dual-carbon rechargeable battery with superior rate property, J. Phys. Chem. C 120 (2016) 22887–22894.

[54] H. Zheng, J. Li, X. Song, G. Liu, V.S. Battaglia, A comprehensive understanding of electrode thickness effects on the electrochemical performances of Li-ion battery

cathodes, Electrochim. Acta 71 (2012) 258–265, https://doi.org/10.1016/j.electacta.2012.03.161.

[55] B. Heidrich, A. Heckmann, K. Beltrop, M. Winter, T. Placke, Unravelling charge/discharge and capacity fading mechanisms in dual-graphite battery cells using an electron inventory model, Energy Storage Mater. 21 (2019) 414–426, https://doi.org/10.1016/j.ensm.2019.05.031.

[56] Y. Sui, C. Liu, R.C. Masse, Z.G. Neale, M. Atif, M. AlSalhi, G. Cao, Dual-ion batteries: the emerging alternative rechargeable batteries, Energy Storage Mater. 25 (2020) 1–32, https://doi.org/10.1016/j.ensm.2019.11.003.